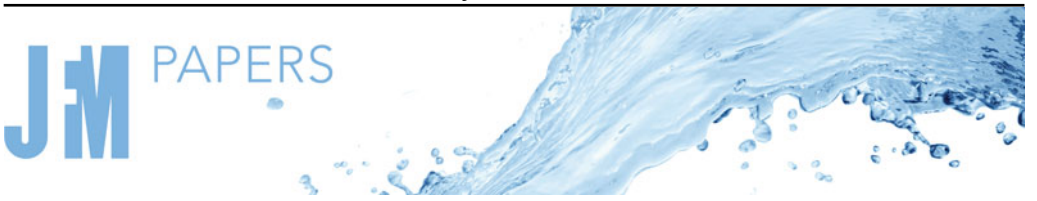
J. Fluid Mech. (2025), *vol.* 1019, A41, doi:10.1017/jfm.2025.10559



Suppressed cascade efficiency by Hall effects in magnetohydrodynamic turbulence

Running Hu[1,2,3], **Jin-Han Xie**[4,5], **Jianchun Wang**[6], **Xinliang Li**[2,3], **Jian Fang**[2], **Yuan Hu**[2] **and Changping Yu**[2]

[1]Institute of Applied Physics and Computational Mathematics, Beijing 100094, PR China

[2]LHD, Institute of Mechanics, Chinese Academy of Sciences, Beijing 100190, PR China

[3]School of Engineering Science, University of Chinese Academy of Sciences, Beijing 100049, PR China

[4]Department of Mechanics and Engineering Science, College of Engineering, Peking University, Beijing 100871, PR China

[5]State Key Laboratory of Turbulence and Complex Systems, College of Engineering, Peking University, Beijing 100871, PR China

[6]Department of Mechanics and Aerospace Engineering, Southern University of Science and Technology, Shenzhen, Guangdong 518055, PR China

Corresponding authors: Jian Fang, jianfang@imech.ac.cn; Yuan Hu, yhu@imech.ac.cn; Changping Yu, cpyu@imech.ac.cn

(Received 28 October 2024; revised 19 May 2025; accepted 7 August 2025)

Magnetohydrodynamic turbulence with Hall effects is ubiquitous in heliophysics and plasma physics. Direct numerical simulations reveal that, when the forcing scale is comparable to the ion inertial scale, the Hall effects induce remarkable cross-helicity. It then suppresses the cascade efficiency, leading to the accumulation of large-scale magnetic energy and helicity. The process is accompanied by the disruption of current sheets through the entrainment by vortex tubes or the excitation of whistler waves. Using the solar wind data from the Parker Solar Probe, the numerical findings are separately confirmed. These findings provide new insights into the emergence of large-scale solar wind turbulence driven by helical fields and Hall effects.

Key words: MHD turbulence, turbulence simulation

1. Introduction

In Hall magnetohydrodynamic (HMHD) turbulence, ion and electron motions become distinct at scales comparable to or smaller than the ion inertial length. This distinction is described by the Hall term in the generalised Ohm's law (Galtier 2016). The HMHD model is thus essential for plasma phenomena such as collisionless magnetic reconnection in the

© The Author(s), 2025. Published by Cambridge University Press.

https://doi.org/10.1017/jfm.2025.10559 Published online by Cambridge University Press

magnetosphere and solar corona (Bhattacharjee 2004; Dorelli *et al.* 2015), kinetic-scale turbulence and energy cascades in the solar wind (Galtier 2006; Gary & Smith 2009), the formation of sharp current sheets and whistler-wave activity (Galtier 2016) and the evolution of magnetised accretion disks and protostellar collapse (Marchand *et al.* 2019; Wurster, Bate & Bonnell 2021).

In the solar corona, strongly helical magnetic fields undergo collisionless reconnection, contributing to transient eruptive phenomena such as coronal mass ejections, which in turn can enhance the solar wind flux (Faganello, Califano & Pegoraro 2008; Servidio *et al.* 2009; Ebrahimi & Raman 2015; Wan *et al.* 2015; Sun *et al.* 2022). The solar wind is a continuous flow of charged particles, mainly electrons and protons. Propagating at speeds from 200 to 800 $\mathrm{km\,s^{-1}}$, it carries a interplanetary magnetic field throughout the heliosphere (Marino & Sorriso-Valvo 2023). Politano & Pouquet (1998) extended the von Kármán–Howarth (vKH) relation (De Karman & Howarth 1938; Kolmogorov 1941) to magnetohydrodynamic (MHD) turbulence. This relation has since been applied to *in situ* measurements to characterise the turbulent properties of the solar wind (Sorriso-Valvo *et al.* 2007; Marino *et al.* 2011, 2012). In addition to these vKH-based analyses, solar wind turbulence has been studied in terms of intermittency and current sheets (Veltri & Mangeney 1999; Bruno *et al.* 2004, 2007; Greco *et al.* 2009; Osman *et al.* 2012; Sorriso-Valvo *et al.* 2015), as well as directional alignments and cellular structuring (Osman *et al.* 2011). The resulting magnetic energy spectrum follows a $k^{-5/3}$ Kolmogorov scaling against the wavenumber k, whereas the kinetic energy spectrum exhibits a $k^{-3/2}$ Iroshnikov–Kraichnan scaling (Alexakis 2013), in agreement with solar wind observations (Podesta, Roberts & Goldstein 2007; Salem *et al.* 2009; Schekochihin 2022). Under a strong guiding field, the perpendicular magnetic spectrum transits from $k_\perp^{-5/3}$ to $k_\perp^{-3/2}$ (Goldreich & Sridhar 1997; Boldyrev 2005, 2006; Chen *et al.* 2020).

In solar wind turbulence, geometric features related to the alignment of the velocity, magnetic field and magnetic potential can be measured through several helicity functions (kinetic, magnetic and cross-helicity) (Galtier 2016). In MHD or HMHD turbulence, besides energy, magnetic helicity is also an inviscid invariant (Elsasser 1956; Woltjer 1958), which quantifies the linkage and twist of magnetic field lines (Galtier 2016). Due to the conservation of energy and its relation to magnetic helicity, magnetic helicity has been found to be inversely cascaded toward large scales (Frisch *et al.* 1975; Alexakis & Biferale 2018). If driven at small scales, the inverse-cascade results in the formation of large-scale magnetic structures, which have been linked to the α-dynamo action (Müller *et al.* 2012; Richner *et al.* 2022). Linkmann & Dallas (2017) explored this inverse cascades using triad-interaction analysis in the Fourier helical decomposition framework, identifying key mechanisms such as the stretch–twist–fold dynamics and small-scale dynamo activity. Aluie & Eyink (2010) introduced the filtering approach to MHD turbulence and found that energy cascades are primarily governed by local interactions, whereas magnetic helicity cascades are dominated by non-local triads. Bian & Aluie (2019) further found the decoupling between the magnetic and kinetic energy cascades. Besides magnetic helicity, cross-helicity also plays a significant role in the turbulent cascades (Galtier 2016). The cross-helicity is defined by the dot product of the velocity and magnetic fields ($\boldsymbol{v}\cdot\boldsymbol{b}$), while interscale cascades are associated with the cross-product ($\boldsymbol{v}\times\boldsymbol{b}$). As the cross-helicity increases, the velocity and magnetic fields align with each other, leading to the suppression of turbulent cascades. Boldyrev (2005, 2006) identified this dynamical alignment as energy transfers to smaller scales in the presence of a guiding magnetic field. This alignment results in a scale-dependent reduction of the nonlinear interaction strength, yielding the $k_\perp^{-3/2}$ Iroshnikov–Kraichnan spectrum (Boldyrev 2006; Chandran,

https://doi.org/10.1017/jfm.2025.10559 Published online by Cambridge University Press

Schekochihin & Mallet 2015). This spectrum has been supported by both numerical simulations and solar wind observations (Mason, Cattaneo & Boldyrev 2008; Perez *et al.* 2012; Chen *et al.* 2020). These spectral results provide indirect evidence of cascade suppression by cross-helicity. More directly, solar wind observations have showed that elevated cross-helicity is associated with the reduced forward energy cascade (Smith *et al.* 2009) and the suppressed turbulence intensity (Marino *et al.* 2012).

At scales approaching the ion inertial length, the ideal MHD framework becomes inadequate, and the HMHD model provides a more suitable description of the underlying dynamics. Galtier (2008) first extended the vKH relation for energy cascades to the HMHD regime. Using numerical data, Ferrand *et al.* (2019) then confirmed the equivalence of several expressions of the vKH relation for energy cascades (Banerjee & Galtier 2016*a*; Hellinger *et al.* 2018; Ferrand *et al.* 2019). Banerjee & Galtier (2016*b*) further derived exact relations for the magnetic helicity under the assumption of homogeneity. Wang & Chkhetiani (2023) established the local vKH relations for the magnetic helicity in both inviscid electron and HMHD turbulence, revealing a Four-thirds law analogous to that for the energy. In a two-dimensional HMHD simulation, Camporeale *et al.* (2018) quantified the relationship between scale-to-scale energy transfers and coherent structures, showing that 50 % of the energy transfer occurs in only 25 % of the spatial domain. Kuzzay, Alexandrova & Matteini (2019) studied the local Kármán–Howarth–Moin relation and highlighted the quasi-one-dimensional or quasi-two-dimensional structures with high cascade rates. Manzini *et al.* (2022) employed the filtering approach to investigate how magnetic reconnection sites contribute to energy dissipation in HMHD turbulence. Additionally, in numerical simulations, Mininni, Gómez & Mahajan (2005) revealed the enhanced growth of large-scale magnetic fields attributed to Hall effects. However, due to the limitations of numerical configurations, the specific and quantitative impact of Hall effects on inverse cascades remains uncertain. Moreover, observational evidence and analysis of the coupling between inverse cascades and Hall effects in solar wind turbulence are still scarce.

In this study, through direct numerical simulations and near-Sun solar wind observations, we investigate the Hall effects on inverse cascades. Our findings reveal that small-scale Hall effects can significantly enhance the magnetic field at larger scales. This enhancement is attributed to the reduced cascade efficiency caused by non-conservative cross-helicity. The paper is organised as follows. We present the details of the simulations and numerical results in § 2. Next, in § 3, the numerical findings are verified using solar wind data from the Parker Solar Probe. Finally, conclusions are presented in § 4.

2. Numerical simulations

2.1. *Numerical set-up*

The governing equations for the velocity $\boldsymbol{v}$ and the magnetic field $\boldsymbol{b}$ are written respectively as follows (Müller *et al.* 2012; Marino & Sorriso-Valvo 2023):

$$\begin{aligned} \partial_t \boldsymbol{v} &= -(\boldsymbol{v}\cdot\boldsymbol{\nabla})\boldsymbol{v} - \boldsymbol{\nabla} p + \boldsymbol{j}\times\boldsymbol{b} + \lambda\Delta^{-1}\boldsymbol{v} - \nu(-\Delta)^{\alpha}\boldsymbol{v} + \boldsymbol{f}_v, \\ \partial_t \boldsymbol{b} &= \boldsymbol{\nabla}\times(\boldsymbol{U}\times\boldsymbol{b}) + \lambda_b\Delta^{-1}\boldsymbol{b} - \eta(-\Delta)^{\alpha}\boldsymbol{b} + \boldsymbol{f}_b, \end{aligned} \tag{2.1}$$

where $\boldsymbol{\nabla}\cdot\boldsymbol{v}=0$, $\boldsymbol{\nabla}\cdot\boldsymbol{b}=0$, p is the fluid pressure, $\boldsymbol{U}=\boldsymbol{v}-d_I\boldsymbol{j}$, $\boldsymbol{j}=\boldsymbol{\nabla}\times\boldsymbol{b}$ is the current density, d_I is the ion inertial length, $\boldsymbol{f}_v$ and $\boldsymbol{f}_b$ are the forcing terms, λ and λ_b are hypo-viscous coefficients for the velocity and magnetic fields, respectively, ν and η are the kinematic viscosity and the magnetic diffusivity, respectively, and α is the hyper-viscous order.

https://doi.org/10.1017/jfm.2025.10559 Published online by Cambridge University Press

Case	Grid	d_I	$\nu = \eta$	α	$\lambda = \lambda_b$	k_f	$\varepsilon_v = \varepsilon_b$
M40	1024^3	—	10^{-4}	1	0.05	40–42	0.015
M40E	512^3	—	2×10^{-4}	1	0.05	40–42	0.015
H40	1024^3	0.05	10^{-4}	1	0.05	40–42	0.015
M100	1024^3	—	1.6×10^{-18}	4	0.05	100–102	0.015
H100	1024^3	0.05	1.6×10^{-18}	4	0.05	100–102	0.015

Table 1. Parameters of the computational configurations. Here, d_I is the ion inertial length, ν and η are the kinematic viscosity and the magnetic diffusivity, respectively, α is the hyper-viscous order, λ and λ_b are hypo-viscous coefficients for the velocity and magnetic fields, respectively, k_f is the forcing wavenumber and ε_v and ε_b are injection rates of kinetic and magnetic energy, respectively.

The code used in this analysis solves the governing equations using the Fourier series in periodic boxes and is developed based on the code for hydrodynamic turbulence (Yan *et al.* 2020; Hu *et al.* 2022). Isotropic white noise forcing schemes ($\boldsymbol{f}_v$ and $\boldsymbol{f}_b$) are applied to the simulation; $\boldsymbol{f}_v$ is non-helical, while $\boldsymbol{f}_b$ is fully helical

$$\frac{\boldsymbol{f}_b \cdot (\boldsymbol{\nabla} \times \boldsymbol{f}_b)}{|\boldsymbol{f}_b||(\boldsymbol{\nabla} \times \boldsymbol{f}_b)|} = 1. \tag{2.2}$$

These forcing schemes only inject magnetic helicity artificially and do not inject any kinetic or cross-helicity. For HMHD cases, due to the short time scale of the Hall effects, we use the split time step for the velocity and magnetic fields to speed up the calculations (Beresnyak 2018).

Five numerical cases are discussed in this paper. The computational parameters are listed in table 1. Cases M40, M40E and M100 are MHD simulations with different forcing wavenumbers k_f, while H40 and H100 are HMHD simulations. All five cases (H40, M40, H100, M100 and M40E) are initially evolved on a 512^3 grid until both the magnetic helicity and total energy reach statistically steady states. Except for M40E, the simulations are then interpolated onto a 1024^3 grid and further evolved for at least 12.4 T_0, where the eddy turnover time is defined as $T_0 = 2\pi/[k_f\sqrt{\langle v_i v_i + b_i b_i\rangle/3}]$. All statistical results reported in this study are averaged over a period of no less than 2.0 T_0.

2.2. *Numerical results*

The spectra of kinetic energy ($E_v(k)$), magnetic energy ($E_b(k)$) and magnetic helicity ($H_M(k)$) are defined by

$$\begin{aligned} E_v(k) &= \sum_{|\boldsymbol{k}|=k} \mathrm{Re}\{\hat{\boldsymbol{v}}(\boldsymbol{k}) \cdot \hat{\boldsymbol{v}}^*(\boldsymbol{k})\}/2, \\ E_b(k) &= \sum_{|\boldsymbol{k}|=k} \mathrm{Re}\{\hat{\boldsymbol{b}}(\boldsymbol{k}) \cdot \hat{\boldsymbol{b}}^*(\boldsymbol{k})\}/2, \\ H_M(k) &= \sum_{|\boldsymbol{k}|=k} \mathrm{Re}\{\hat{\boldsymbol{a}}(\boldsymbol{k}) \cdot \hat{\boldsymbol{b}}^*(\boldsymbol{k})\}, \end{aligned} \tag{2.3}$$

where $\hat{\cdot}$ represents the values in spectral space, the superscript $*$ represents the conjugate value, $\hat{\boldsymbol{a}}(\boldsymbol{k}) = [\mathrm{i}\boldsymbol{k} \times \hat{\boldsymbol{b}}(\boldsymbol{k})]/|\boldsymbol{k}|^2$ is the magnetic potential, i denotes the imaginary unit, Re and Im represent the real and imaginary parts of a complex value.

The spectra $E_v(k)$, $E_b(k)$ and $H_M(k)$ are given in figure 1. The kinetic energy spectra $E_v(k) \sim k^{-3/2}$, the magnetic energy spectra $E_b(k) \sim k^{-5/3}$ and the magnetic helicity

https://doi.org/10.1017/jfm.2025.10559 Published online by Cambridge University Press

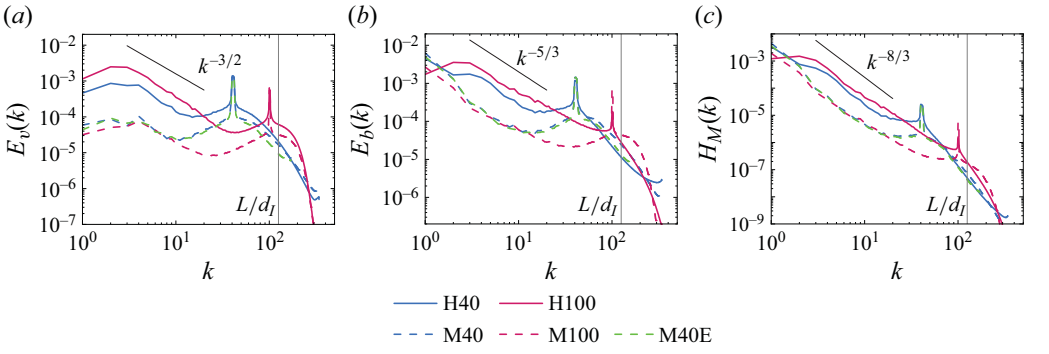


Figure 1. Spectra. (*a*) Kinetic energy spectrum $E_v(k)$. (*b*) Magnetic energy spectrum $E_b(k)$. (*c*) Magnetic helicity spectrum $H_M(k)$. Here, L/d_I is the ion inertial scale d_I normalised by the computational domain scale L.

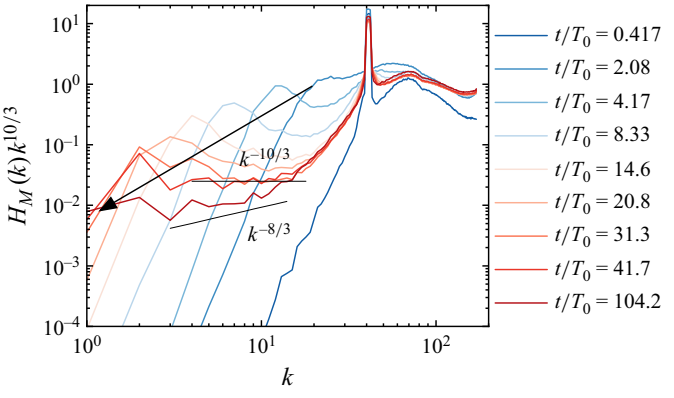


Figure 2. Evolution of $H_M(k)k^{10/3}$ for M40E. Time increases along the arrow, and the values are given in the legend after normalisation by the eddy turnover time T_0.

spectra $H_M(k) \sim k^{-8/3} \sim E_b(k)/k$, implying that the magnetic field is fully helical. In comparison, only a slope around $k^{-10/3}$ has been reported based on unsteady numerical simulations with hyper-viscosity (Müller *et al.* 2012; Linkmann & Dallas 2017). Therefore, an evolutionary case M40E with a relatively lower grid resolution of 512^3 is given here for verification. The evolution of the magnetic helicity spectra $H_M(k)$ is given in figure 2. The time is normalised by the eddy turnover time T_0. As time evolves, $H_M(k) \sim k^{-10/3}$ when $t/T_0 \in [8.33, 41.7]$, but $H_M(k) \sim k^{-8/3}$ at $t/T_0 = 104.0$. The comparison further verifies the validity of our data.

In figure 1, a comparison between the MHD and HMHD cases shows that Hall effects enhance large-scale magnetic energy and helicity by nearly an order of magnitude. This indicates that the ion-scale dynamics continues to influence the magnetic field at larger scales, which is the main finding of this study.

To understand the mechanism behind the magnetic field enhancement, the cascade rates should be measured. The filtering approach (Aluie & Eyink 2010; Aluie 2017; Camporeale *et al.* 2018; Manzini *et al.* 2022) is employed to examine the scale-dependent features of the cascades. Different filter functions have been shown to yield qualitatively consistent results (Kuzzay *et al.* 2019; Yan *et al.* 2020). The fourth-order Butterworth filter (Camporeale *et al.* 2018) is used in this study. The interscale flux for kinetic energy cascades can be

https://doi.org/10.1017/jfm.2025.10559 Published online by Cambridge University Press

written as

$$\widetilde{\Pi}_{Ev} = -\epsilon_{ijk}\left[\tilde{v}_i \tau_{jk}(\boldsymbol{v}, \boldsymbol{\omega}) + \tilde{v}_i \tau_{jk}(\boldsymbol{j}, \boldsymbol{b})\right], \tag{2.4}$$

where the vorticity $\boldsymbol{\omega} = \nabla \times \boldsymbol{v}$, ϵ_{ijk} is the Levi-Civita symbol, $\boldsymbol{\tau}_{ij}(\boldsymbol{p}, \boldsymbol{q}) = \widetilde{p_i q_j} - \widetilde{p}_i \widetilde{q}_j$ and the superscript $\tilde{\cdot}$ represents a filtered quantity. The interscale flux for the magnetic energy cascades can be written as

$$\begin{aligned} \widetilde{\Pi}_{Eb1} &= -\epsilon_{ijk}\tilde{j}_i \tau_{jk}(\boldsymbol{v}, \boldsymbol{b}), \\ \widetilde{\Pi}_{Eb2} &= \epsilon_{ijk} d_I \tilde{j}_i \tau_{jk}(\boldsymbol{j}, \boldsymbol{b}), \\ \widetilde{\Pi}_{Eb} &= \widetilde{\Pi}_{Eb1} + \widetilde{\Pi}_{Eb2}. \end{aligned} \tag{2.5}$$

The interscale flux for magnetic helicity cascades can be written as

$$\begin{aligned} \widetilde{\Pi}_{HM1} &= -2\epsilon_{ijk}\tilde{b}_i \tau_{jk}(\boldsymbol{v}, \boldsymbol{b}), \\ \widetilde{\Pi}_{HM2} &= 2\epsilon_{ijk} d_I \tilde{b}_i \tau_{jk}(\boldsymbol{j}, \boldsymbol{b}), \\ \widetilde{\Pi}_{HM} &= \widetilde{\Pi}_{HM1} + \widetilde{\Pi}_{HM2}. \end{aligned} \tag{2.6}$$

Here, $\widetilde{\Pi}_{Eb1}$ and $\widetilde{\Pi}_{HM1}$ are the MHD terms, while $\widetilde{\Pi}_{Eb2}$ and $\widetilde{\Pi}_{HM2}$ are the Hall terms.

Figures 3 (a) and 3(b) show the kinetic energy fluxes $\langle \widetilde{\Pi}_{Ev} \rangle$, where $\langle \cdot \rangle$ represents the ensemble average. The inverse cascades of $\langle \widetilde{\Pi}_{Ev} \rangle$ are negligible, and the Hall effects have minimal impact on the kinetic energy fluxes. The magnetic energy flux $\langle \widetilde{\Pi}_{Eb} \rangle$ and its decomposition are shown in figures 3 (c) and 3(d). As shown, most magnetic energy cascades forward toward small scales. Regardless of the forcing wavenumber, the Hall term $\langle \widetilde{\Pi}_{Eb2} \rangle$ dominates at small scales ($\Delta/L \lessapprox 10^{-2}$), which is attributed to its higher-order nature. Weak inverse cascades appear and are linked to the α-dynamo action (Müller *et al.* 2012; Linkmann & Dallas 2017; Pouquet *et al.* 2019). Hall effects also have little influence on the inverse-cascade rates of magnetic energy. Figures 3 (e) and 3(f) show the mean magnetic helicity flux $\langle \widetilde{\Pi}_{HM} \rangle$ and its decomposition. The component $\langle \widetilde{\Pi}_{HM1} \rangle$ is dominant, with most magnetic helicity cascading inversely toward large scales.

Hall effects have a minimal impact on the inverse cascades shown in figure 3, but strongly enhance the large-scale velocity and magnetic fields shown in figure 1. This means that, to maintain the same cascade rates, magnetic fields must be much stronger, implying that cascades are less efficient in HMHD cases. Since large scales are dominated by inverse magnetic helicity cascades, the dominant term $\widetilde{\Pi}_{HM1}$ will henceforth be the focus. According to the definitions (2.5) and (2.6), the local fluxes $\widetilde{\Pi}_{Eb1}$ and $\widetilde{\Pi}_{HM1}$ are associated with the cross-product of the velocity and magnetic fields ($\boldsymbol{v} \times \boldsymbol{b}$), while the cross-helicity is defined by $\boldsymbol{v} \cdot \boldsymbol{b}$. As the cross-helicity increases, the velocity and magnetic fields align with each other, which could suppress the efficiency of $\widetilde{\Pi}_{Eb1}$ and $\widetilde{\Pi}_{HM1}$. Figure 4 shows the cross-helicity spectra $H_C(k)$, defined as follows:

$$H_C(k) = \sum_{|\boldsymbol{k}|=k} \mathrm{Re}\{\hat{\boldsymbol{v}}(\boldsymbol{k}) \cdot \hat{\boldsymbol{b}}^*(\boldsymbol{k})\}. \tag{2.7}$$

As shown, $H_C(k)$ is approximately zero for the MHD cases but negative for the HMHD cases. In fact, for the MHD cases, the cross-helicity is conservative (Galtier 2016). No cross-helicity is injected, making it inherently zero. In contrast, for the HMHD cases, due to the generalised helicity, the weighted sum of kinetic and cross-helicity is conservative (Galtier 2016). The kinetic helicity is transformed to cross-helicity through the Hall effects. Physically, Hall effects arise from the ion cyclotron dynamics of the magnetic field induced by the Lorentz force. In the MHD cases, only the ion cyclotron effects on the

https://doi.org/10.1017/jfm.2025.10559 Published online by Cambridge University Press

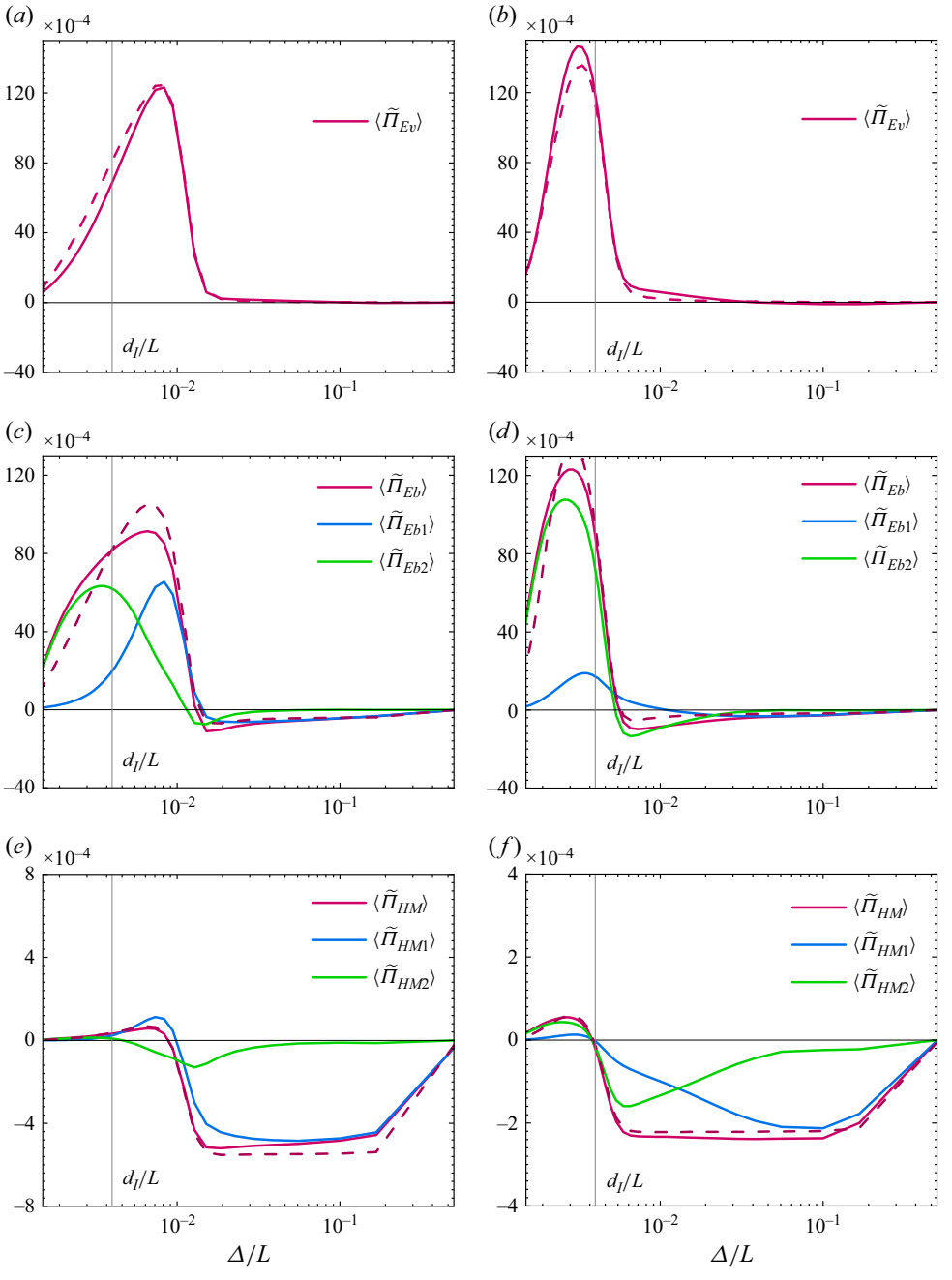


Figure 3. Fluxes versus the filter width Δ. Here, Δ is normalised by the computational domain scale L. (*a*,*b*) Kinetic energy fluxes for (*a*) H40 and M40, (*b*) H100 and M100. (*c*,*d*) Magnetic energy fluxes for (*c*) H40 and M40, (*d*) H100 and M100. (*e*,*f*) Magnetic helicity fluxes for (*e*) H40 and M40, (*f*) H100 and M100. Solid lines: HMHD cases; dashed lines: MHD cases.

velocity are considered. In the HMHD cases, the inclusion of ion cyclotron effects on the magnetic field, which couples the chiralities of the velocity and magnetic fields, leads to the generation of non-zero cross-helicity. Excluding the magnitude effects, the normalised

https://doi.org/10.1017/jfm.2025.10559 Published online by Cambridge University Press

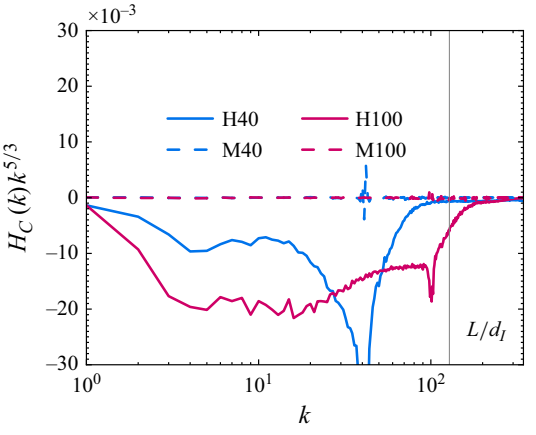


Figure 4. Compensated spectrum of cross-helicity $H_C(k)k^{5/3}$. Solid lines: HMHD cases; dashed lines: MHD cases.

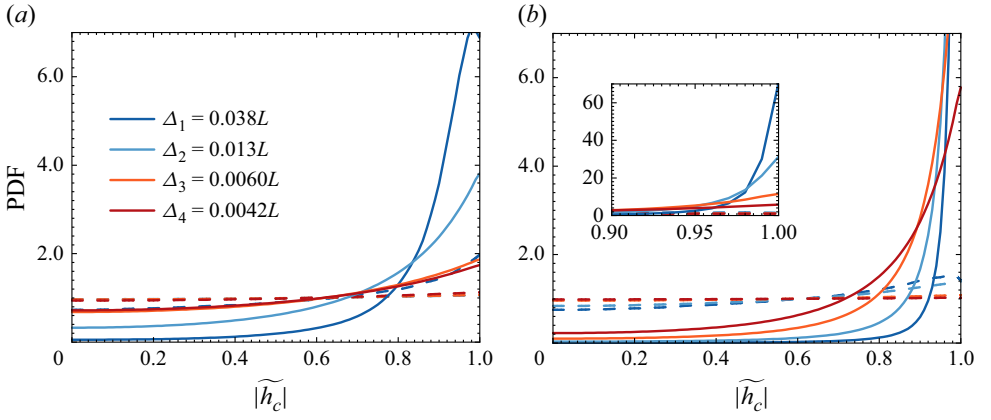


Figure 5. Probability distribution functions of $|\widetilde{h_c}|$ for (*a*) H40 and M40, (*b*) H100 and M100. Solid lines: HMHD cases; dashed lines: MHD cases. The inset in (*b*) shows the local details.

cross-helicity can be defined by

$$|\widetilde{h_c}| = |\widetilde{\boldsymbol{v}} \cdot \widetilde{\boldsymbol{b}}|/|\widetilde{\boldsymbol{v}}||\widetilde{\boldsymbol{b}}|, \tag{2.8}$$

which directly measures the alignment between the velocity and magnetic fields. Figure 5 shows the probability distribution functions (PDF) of $|\widetilde{h_c}|$ with four typical filter widths. As the filter width increases or the Hall effects are introduced, $|\widetilde{h_c}|$ approaches 1.0, indicating enhanced alignments between $\widetilde{\boldsymbol{v}}$ and $\widetilde{\boldsymbol{b}}$.

The joint PDF of the magnetic helicity flux $\widetilde{\Pi}_{HM1}$ and the normalised cross-helicity $|\widetilde{h_c}|$ are given in figure 6. For M40 and M100, $\widetilde{\Pi}_{HM1}$ is almost independent of $|\widetilde{h_c}|$. In contrast, when Hall effects are introduced (H40 and H100), $\widetilde{\Pi}_{HM1}$ is primarily concentrated in the region with significant $|\widetilde{h_c}|$, indicating a potential reduction in efficiency. For a quantitative estimation, a direct definition of the efficiency Γ_{HM1} for magnetic helicity cascades is

https://doi.org/10.1017/jfm.2025.10559 Published online by Cambridge University Press

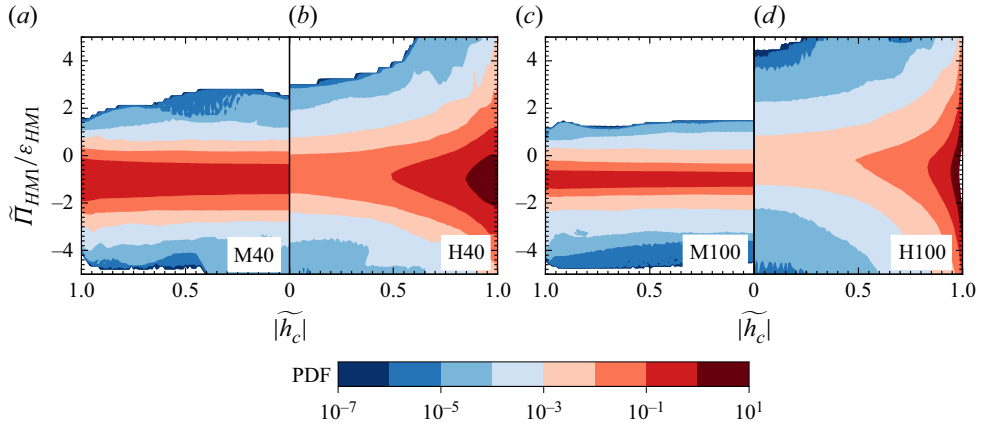


Figure 6. Joint PDF of the normalised magnetic helicity flux $\widetilde{\Pi}_{HM1}/\varepsilon_{HM1}$ and the normalised cross-helicity $|\widetilde{h_c}|$ with $\Delta = 0.038L$ for (*a*) H40 and M40, (*b*) H100 and M100. Here, ε_{HM1} is the magnetic helicity cascade rate.

introduced as

$$\Gamma_{HM1} = \frac{|\widetilde{\Pi}_{HM1}|}{2|\widetilde{\boldsymbol{v}}||\widetilde{\boldsymbol{b}}|^2} = \underbrace{\frac{|\widetilde{\Pi}_{HM1}|}{2|\widetilde{\boldsymbol{b}}||\widetilde{\boldsymbol{m}}|}}_{\cos(\widetilde{\boldsymbol{b}},\widetilde{\boldsymbol{m}})} \underbrace{\frac{|\widetilde{\boldsymbol{v}}\times\widetilde{\boldsymbol{b}}|}{|\widetilde{\boldsymbol{v}}|\,|\widetilde{\boldsymbol{b}}|}}_{\sin(\widetilde{\boldsymbol{b}},\widetilde{\boldsymbol{v}})} \underbrace{\frac{|\widetilde{\boldsymbol{m}}|}{|\widetilde{\boldsymbol{v}}\times\widetilde{\boldsymbol{b}}|}}_{C_\Delta}, \tag{2.9}$$

where

$$\widetilde{\boldsymbol{m}} = \epsilon_{ijk}\tau_{jk}(\boldsymbol{v},\boldsymbol{b})\boldsymbol{e}_i, \tag{2.10}$$

and $\boldsymbol{e}_i$ is the unit vector on the ith direction. The decomposition is based on the fact that $\widetilde{\Pi}_{HM1}$ is the mixed product of the vector $\widetilde{\boldsymbol{b}}$ and the second-order tensor $\tau_{ij}(\widetilde{\boldsymbol{v}},\widetilde{\boldsymbol{b}})\boldsymbol{e}_i\boldsymbol{e}_j$. Therefore, $\cos(\widetilde{\boldsymbol{b}},\widetilde{\boldsymbol{m}})$ and $\sin(\widetilde{\boldsymbol{b}},\widetilde{\boldsymbol{v}})$ evaluate the efficiency loss induced by the angles between tensors in the mixed product. The parameter C_Δ is a necessary correction factor induced by replacing $\widetilde{\boldsymbol{m}}$ with $\widetilde{\boldsymbol{v}}\times\widetilde{\boldsymbol{b}}$ in $\sin(\widetilde{\boldsymbol{b}},\widetilde{\boldsymbol{v}})$. The replacement is performed for the specific definition of the geometric alignment between $\widetilde{\boldsymbol{b}}$ and $\widetilde{\boldsymbol{v}}$. Figure 7 shows the conditional average of the cascade efficiency with respect to $|\widetilde{h_c}|$. As shown, $\cos(\widetilde{\boldsymbol{b}},\widetilde{\boldsymbol{m}})$ is nearly independent of $|\widetilde{h_c}|$ but inversely proportional to the Hall effects and $\sin(\widetilde{\boldsymbol{b}},\widetilde{\boldsymbol{v}})$ is inversely proportional to $|\widetilde{h_c}|$ but independent of the Hall effects, consist with its definition. The value of C_Δ is proportional to $|\widetilde{h_c}|$ and the Hall effects. In total, when $|\widetilde{h_c}| \sim 0$, the Hall effects on $\cos(\widetilde{\boldsymbol{b}},\widetilde{\boldsymbol{m}})$ and C_Δ compensate for each other, causing the cascade efficiency Γ_{HM1} to be independent of the Hall effects. However, when $|\widetilde{h_c}| \sim 1.0$, the cascade efficiency Γ_{HM1} is strongly reduced by the Hall effects, which is mainly attributed to the alignment between $\widetilde{\boldsymbol{v}}$ and $\widetilde{\boldsymbol{b}}$. Specifically, with $\Delta = 0.038L$, for H40 and M40, Hall effects reduce the mean efficiency $\langle\Gamma_{HM1}\rangle$ by 37.9 %.

In comparison, both the kinetic helicity in the hydrodynamic turbulence (Chen, Chen & Eyink 2003; Yan *et al.* 2020) and the cross-helicity in the HMHD turbulence could affect the cascade efficiencies. It could be worthwhile to investigate the disparities between the effects induced by the two types of helicity. Generally, kinetic or cross-helicity has two sources: geometric and phase alignments (Milanese, Loureiro & Boldyrev 2021). With the cross-helicity as an example, geometric alignment means a direct increase in $|\widetilde{h_c}|$, while phase alignment is a transformation from negative $\widetilde{h_c}$ to positive $\widetilde{h_c}$.

https://doi.org/10.1017/jfm.2025.10559 Published online by Cambridge University Press

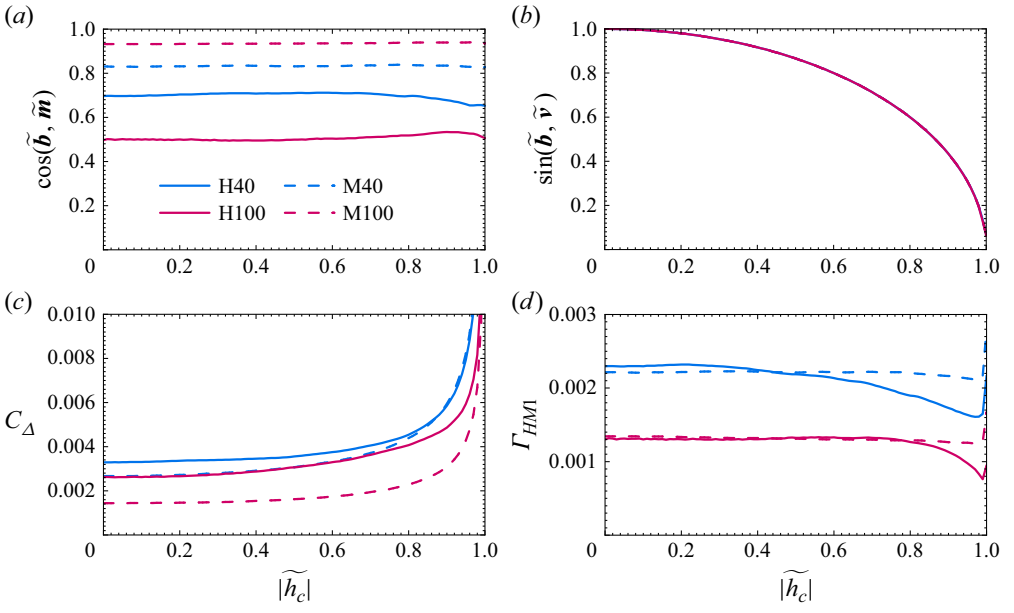


Figure 7. Conditional average of cascade efficiency versus the normalised cross-helicity $|\widetilde{h_c}|$ with $\Delta = 0.038L$. Panels show (*a*) $\cos(\boldsymbol{b}, \boldsymbol{m})$, (*b*) $\sin(\boldsymbol{b}, \boldsymbol{v})$, (*c*) C_Δ, (*d*) Γ_{HM1}.

In hydrodynamic turbulence, the kinetic helicity cascades forward with dynamic phase alignments, while no geometric alignment is detected (Milanese *et al.* 2021). In comparison, figure 5 reveals that geometric alignments are the key processes in HMHD turbulence. The two different alignments lead to different effects on the cascades. As shown in figure 7, the geometric alignment of the cross-helicity induced by Hall effects strongly reduces the cascade efficiency. In hydrodynamic flows, because of the lacking geometric alignments, such suppression of the cascade efficiency has not been observed in homogeneous isotropic turbulence (Alexakis 2017; Alexakis & Biferale 2018). However, similar suppression may occur under conditions such as artificial restriction of nonlinear triads (Biferale *et al.* 2012, 2013; Sahoo & Biferale 2015), or in the presence of external factors like specialised forcing (Plunian *et al.* 2020) or background rotation (Buzzicotti *et al.* 2018; Hu *et al.* 2022).

Figure 8 presents the magnitude of the current density, $|\boldsymbol{j}|$, with the magnetic field lines and streamlines shown in pink and green, respectively. In conventional MHD turbulence (M40), typical current sheets are sustained. However, when Hall effects are introduced (H40), these sheets are completely disrupted due to the alignment between the velocity and magnetic fields. The resulting current density distribution becomes irregular and coarse. The intermittency of the current density is quantified in figure 9 using the PDF and the flatness factor $F(\Delta)$, where $F(\Delta)$ is defined as

$$F(\Delta) = \left\langle \sum_{i=1}^{3} \widetilde{j}_i^4 \right\rangle \Big/ \left\langle \sum_{i=1}^{3} \widetilde{j}_i^2 \right\rangle^2 . \tag{2.11}$$

As shown in figure 9, with the inclusion of Hall effects, the intermittency is reduced. Especially, the current density in H100 with $\Delta = 0.038L$ exhibits an almost Gaussian distribution. This suppression on intermittency is consistent with previous numerical findings (Martin *et al.* 2013; Yadav, Miura & Pandit 2022) and observations of the solar

https://doi.org/10.1017/jfm.2025.10559 Published online by Cambridge University Press

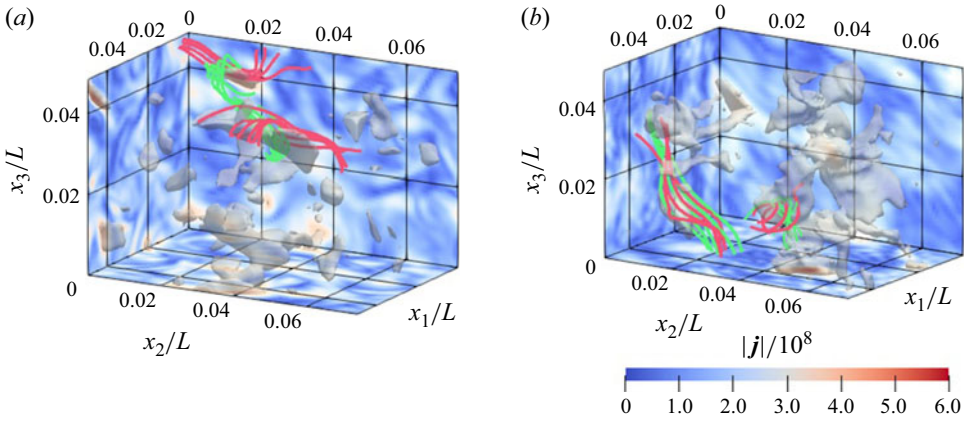


Figure 8. Structures with $|\boldsymbol{j}| > 2.2\,\mathrm{mean}\{|\boldsymbol{j}|\}$. The background slice shows the contour of $|\boldsymbol{j}|$. Panels show (*a*) M40; (*b*) H40. Pink lines: magnetic lines; green lines: streamlines.

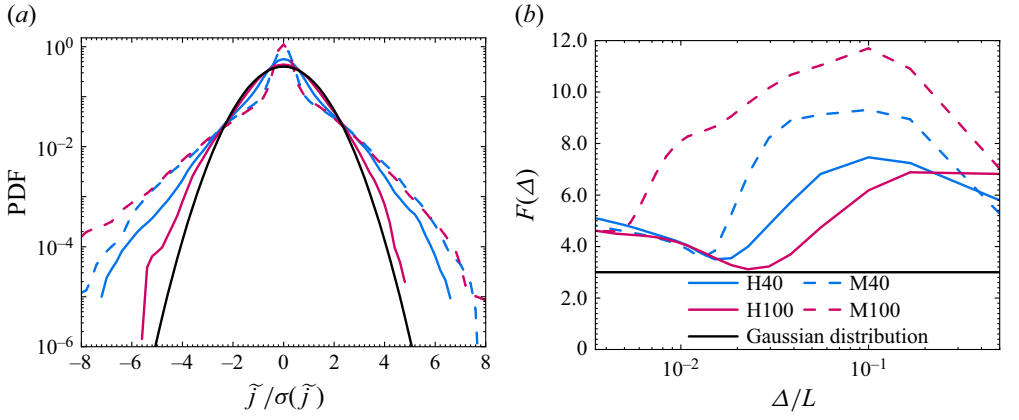


Figure 9. Intermittency of current density. (*a*) The PDF of filtered current density with $\Delta = 0.038L$. (*b*) Flatness of current density versus the filter width Δ.

wind (Kiyani *et al.* 2009). It reflects the widening of the macroscale and the breakdown of intermittent sheets (Martin *et al.* 2013). The disruption of current sheets can be attributed to filamentation, resulting from either the entrainment of sheets by vortex tubes or the excitation of whistler waves (Martin *et al.* 2013; Miura & Araki 2014; Miura 2024).

3. Solar wind observations

3.1. *Data processing*

To verify our findings with solar wind data, we evaluate the one-second-resampled time series from the Parker Solar Probe (PSP) project (Bale *et al.* 2016; Fox *et al.* 2016; Case *et al.* 2020; Raouafi *et al.* 2023). The data from 1 to 10 November 2018, ranging from 0.16 to 0.24 AU, are used for this analysis. We resample all variables to 1 Hz to create a uniform time series.

Figure 10 shows the time series of the basic data. As shown, the heliocentric distance ranges from 0.16 to 0.24 AU. The proton number density n, components of the velocity field $\boldsymbol{v}$ and components of the magnetic field $\boldsymbol{B}$ are shown in figure 10

https://doi.org/10.1017/jfm.2025.10559 Published online by Cambridge University Press

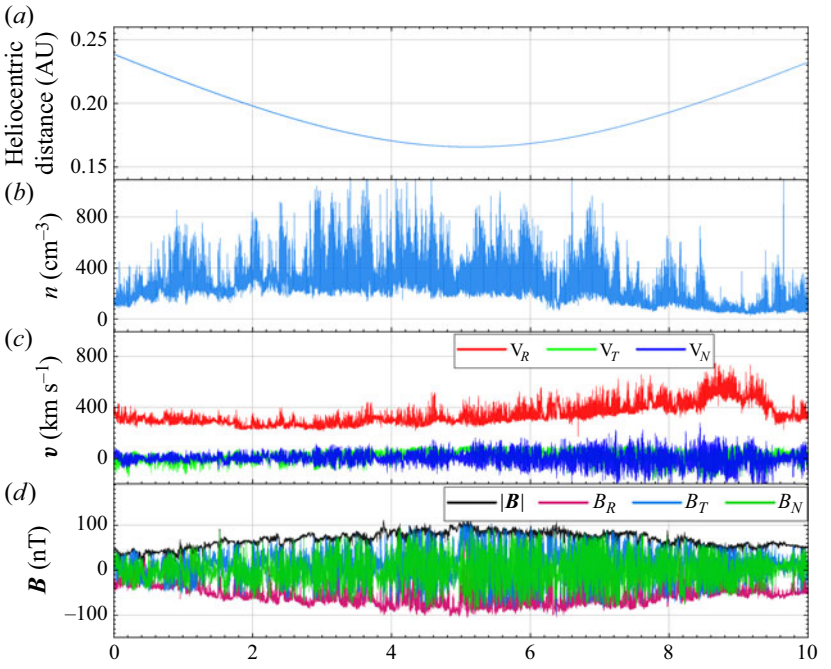


Figure 10. Basic data for 1–10 November 2018 from the PSP. (*a*) Heliocentric distance. (*b*) Proton number density n. (*c*) Velocity field. The subscripts R,T and N represent the radial, tangential and normal components, respectively. (*d*) Magnetic field. $|\boldsymbol{b}|$ denotes the magnetic field magnitude.

(*b–d*), respectively. The main averages are summarised as follows: $\langle n\rangle_t = 260.6\,\mathrm{cm}^{-3}$, $V_R = \langle v_R\rangle_t = 341.5\,\mathrm{km\ s}^{-1}$ and $\langle|\boldsymbol{B}|\rangle_t = 68.8\,\mathrm{nT}$, where $\langle\cdot\rangle_t$ represents the time average, and V_R is the mean radial velocity.

Using the Taylor hypothesis (Taylor 1938), the newly derived vKH relation for the magnetic helicity cascades in the HMHD turbulence can be written as

$$\begin{aligned} V_{HM}(\tau) &= \left\langle -V_R\tau\delta(v_N b_T - v_T b_N)\delta b_R/2 - d_I\delta(b_R b_i)b_i^*\right\rangle_t \\ &= \varepsilon_{HM} V_R \tau/3, \end{aligned} \tag{3.1}$$

where V_R is the mean radial velocity, τ is the time lag, δq represents two-point increments for any variable q, subscripts R,T and N represent the radial, tangential and normal components, respectively, and ε_{HM} is the estimated magnetic cascade rates. The magnetic field $\boldsymbol{b}$ is normalised as

$$\boldsymbol{b} = \boldsymbol{B}/(\mu_0 m_0 n)^{-1/2}, \tag{3.2}$$

where μ_0 is the magnetic permeability of vacuum, m_0 is the proton mass and n is the proton number density. The vKH relation (3.1) is derived in the strictly incompressible case, and n is assumed to be constant. See Appendix A for the theoretical derivation. To avoid overestimating the effects of Alfvén speed gradients, the density is averaged over several correlation times (1250 s) to suppress local fluctuations (Bandyopadhyay *et al.* 2020). In addition, we remove some spurious spikes from the dataset, which are remnants of poor-quality fits. These spikes are excluded using a Hampel filter with a sliding window of 10 points and a threshold of three times the local standard deviation (Bandyopadhyay *et al.* 2018, 2020; Brodiano, Dmitruk & Andrés 2023). After this preprocessing, turbulence analysis is performed on the PSP dataset. The data have a cadence of 1 s and are analysed

https://doi.org/10.1017/jfm.2025.10559 Published online by Cambridge University Press

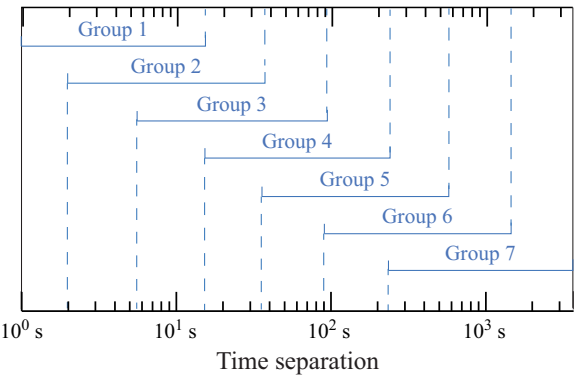


Figure 11. Time separation groups used to identify the linear scaling of the vKH relation.

over 8.6×10^5 overlapping windows, each 1 h in duration. Time separations from 1 s to 1 h are considered in the analysis. In practice, it is challenging to identify a clear linear scaling over the entire range of time separations. To address this problem, as shown in figure 11, the whole time separations are divided into seven overlapping groups, each spanning over one decade. This ensures sufficient range for identifying potential linear scaling and facilitates the determination of the specific scales over which the magnetic helicity cascade becomes evident.

Additionally, to recognise the cascade direction of the magnetic helicity, the magnetic helicity should be calculated. In the PSP data, only single-point measurement is available. When calculating the magnetic helicity, the difficulty is in evaluating the magnetic potential field $\boldsymbol{a}$. Under the assumption of isotropy, Matthaeus & Goldstein (1982) obtained the magnetic helicity (H_M) spectrally. The same approach is adopted here to measure magnetic helicity. To examine its relationship with cross-helicity, we also evaluate the cross-helicity using this method. Accordingly, for each time series, the magnetic and cross-helicities are evaluated, respectively, as

$$\begin{aligned} H_M &= \left\langle \sum_k 4\mathrm{Im}\{\hat{b}_2\hat{b}_3\}/k \right\rangle_t, \\ H_C &= \left\langle \sum_k \mathrm{Re}\{\hat{\boldsymbol{v}} \cdot \hat{\boldsymbol{b}}^*\} \right\rangle_t, \end{aligned} \tag{3.3}$$

where $\hat{\cdot}$ represents the quantities in spectral space, Im and Re represent the imaginary and real parts of a complex value, respectively.

3.2. *Data evaluation*

With the newly derived vKH relation (3.1), the magnetic helicity cascade rates can be estimated as

$$\varepsilon_{HM} = V_R\, \tau/[3V_{HM}(\tau)]. \tag{3.4}$$

Figure 12 presents two typical examples exhibiting the standard magnetic helicity cascades. As shown in figure 12 (*b*), on 8 November 2018, from 21:11 to 22:11, $V_{HM}(\tau)$ is linear for nearly two decades with $\varepsilon_{HM} = 1.23 \times 10^{13}$ J m (kg s)$^{-1}$. Figure 13 shows the PDF of $|\varepsilon_{HM}|$, with a mean value of 2.79×10^{12} J m (kg s)$^{-1}$.

https://doi.org/10.1017/jfm.2025.10559 Published online by Cambridge University Press

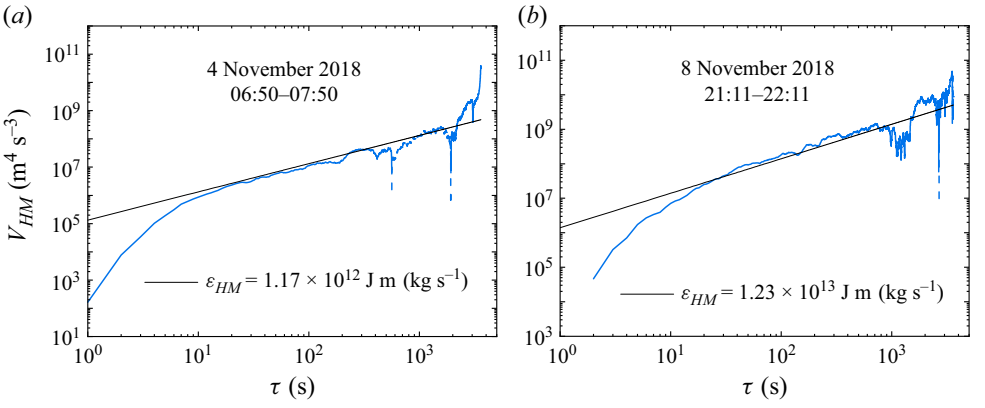


Figure 12. Two examples of magnetic helicity cascades on (*a*) 4 November 2018, 6:50–7:50 and (*b*) 8 November 2018, 21:11–22:11. Here, ε_{HM} denotes the estimated magnetic cascade rate.

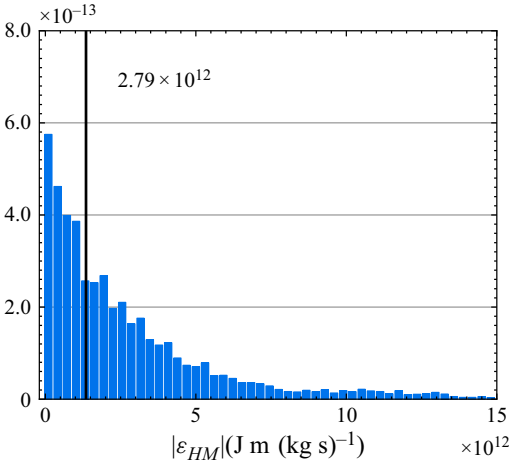


Figure 13. Probability distribution functions of the magnetic cascade rates. The black solid line shows the mean magnetic helicity cascade rate.

Notably, the cross-helicity observed in the solar wind may also originate from mechanisms other than the Hall effect. Therefore, the numerical findings are assessed here in two aspects: the generation of cross-helicity and the suppression of cascade efficiency associated with it. Conditioned by the cascade direction, the relation between the cross-helicity (H_C) and the magnetic helicity (H_M) is shown in figure 14 (*a*). Regardless of the type of the cascade, strong cross-helicity is observed alongside a magnetic helicity cascade. Figure 14 (*b*) shows the cascade efficiency $\Gamma_{HMt} = |\varepsilon_{HM}|/[|\delta \boldsymbol{v}||\delta \boldsymbol{b}|^2]$ versus the normalised cross-helicity $|h_{ct}| = |\delta \boldsymbol{v} \cdot \delta \boldsymbol{b}|/|\delta \boldsymbol{v}||\delta \boldsymbol{b}|$. Here, $|\delta \boldsymbol{v} \cdot \delta \boldsymbol{b}|$, $|\delta \boldsymbol{v}|$ and $|\delta \boldsymbol{b}|$ are averaged over the time separation group corresponding to magnetic helicity cascades (figure 11). As shown, the normalised cascade rate Γ_{HMt} is suppressed by $|h_{ct}|$, consistent with the numerical findings of this study.

4. Conclusions

In this paper, we use numerical simulations and solar wind data to investigate Hall effects on inverse cascades. We find that Hall effects could induce strong cross-helicity through

https://doi.org/10.1017/jfm.2025.10559 Published online by Cambridge University Press

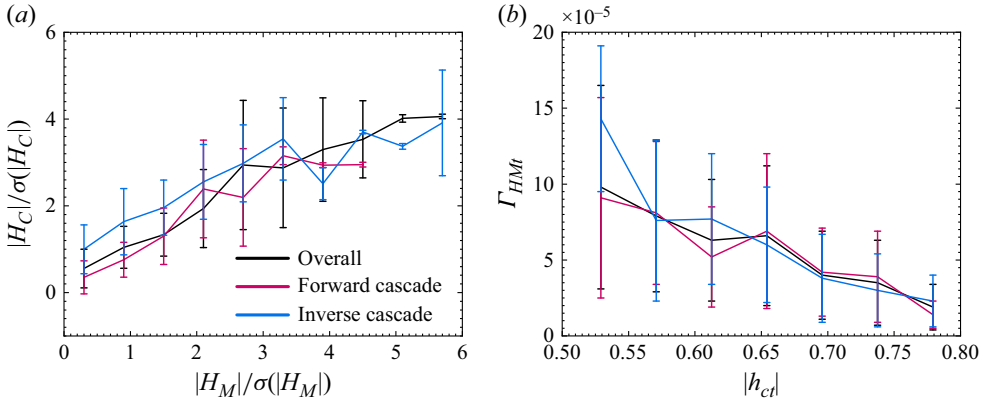


Figure 14. Results from the solar wind data. (*a*) Relation between the cross-helicity H_C and the magnetic helicity H_M. Here, σ represents the variance. (*b*) Cascade efficiency Γ_{HMt} versus the normalised cross-helicity $|h_{ct}|$.

geometric alignments between the velocity and magnetic fields. The cross-helicity then significantly reduces the inverse-cascade efficiencies and leads to the accumulation of magnetic energy and helicity at large scales. The process is associated with the disruption of current sheets due to the entrainment of sheets by vortex tubes or the excitation of whistler waves. Then, the numerical findings about the cross-helicity generation and the cascade efficiency suppression are separately confirmed by the solar wind observations from the PSP. In hydrodynamic turbulence, the turbulent strength on the inertial scale is solely determined by the cascade rates, and the Kolmogorov coefficient is universal for turbulent flows (Pope 2000). However, the present results suggest that such universality may not hold in HMHD turbulence exhibiting inverse cascades. The turbulent intensity within the inverse-cascade range may be amplified by the presence of cross-helicity and Hall effects.

In the heliosphere, some extreme solar wind events originate from dynamic processes in the solar corona, where magnetic helicity and Hall effects play important roles. It is generally accepted that Hall effects can be assumed to be negligible at large scales in the solar wind (Marino & Sorriso-Valvo 2023), which justifies the use of MHD models at these scales. However, this study proposes a new mechanism in solar wind turbulence whereby Hall effects can significantly influence the large-scale magnetic field through cross-helicity. This mechanism may help explain how solar wind turbulence at larger scales can be strongly affected by processes occurring at the ion inertial scale, especially during extreme solar wind events with strongly helical magnetic fields.

Funding. This work was supported by the National Natural Science Foundation of China (Grants No. 12472229, No. 12072349, No. 12232018, No. 91852203, No. 12202457, No. 92052102 and No. 12272006) and the National Key Research and Development Program of China (Grant No. 2020YFA0711800).

Declaration of interests. The authors report no conflict of interest.

Appendix A. Derivation of two vKH relations for magnetic helicity

A.1. *First vKH relation for the magnetic helicity*

The governing equation for the magnetic potential $\boldsymbol{a}$ is

$$\partial_t \boldsymbol{a} = \boldsymbol{U} \times \boldsymbol{b} + 2\nabla\psi + \lambda_b \Delta^{-1}\boldsymbol{b} - \eta(-\Delta)^{\alpha}\boldsymbol{a} + \boldsymbol{f}_a, \tag{A1}$$

where $2\nabla\psi$ corresponds to an arbitrary choice of gauge, and $\nabla \times \boldsymbol{f}_a = f_b$.

https://doi.org/10.1017/jfm.2025.10559 Published online by Cambridge University Press

For three arbitrary vectors $\boldsymbol{p}$, $\boldsymbol{q}$ and $\boldsymbol{o}$, the isotropic second- and third-order isotropic tensors without reflection symmetry ($R_{ij}^{pq} = \langle p_i(\boldsymbol{x}) q_j(\boldsymbol{x}')\rangle$ and $\Phi_{ijl}^{opq} = \langle o_i(\boldsymbol{x}) p_j(\boldsymbol{x}) q_l(\boldsymbol{x})'\rangle$) can be written as (Politano, Gomez & Pouquet 2003)

$$\begin{aligned} R_{ij}^{pq}(\boldsymbol{r}) &= A^{pq}(r) r_i r_j + B^{pq}(r)\delta_{ij} + \bar{C}^{pq}(r)\epsilon_{ijl} r_l, \\ \Phi_{ijl}^{opq}(\boldsymbol{r}) &= a_{11}(r) r_l \delta_{ij} + a_{12}(r) r_j \delta_{il} + a_{13}(r) r_i \delta_{jl} \\ &\quad + a_3(r) r_i r_j r_l + \bar{b}_{23}(r) r_i \epsilon_{jlm} r_m + \bar{b}_{22}(r) r_j \epsilon_{lim} r_m \\ &\quad + \bar{b}_{21}(r) r_l \epsilon_{ijm} r_m, \end{aligned} \tag{A2}$$

where $\boldsymbol{r} = \boldsymbol{x}' - \boldsymbol{x}$ is the displacement between two positions $\boldsymbol{x}$ and $\boldsymbol{x}'$ with a distance $r = |\boldsymbol{r}|$, δ_{ij} represents the Kronecker delta, ϵ_{ijl} is the Levi-Civita symbol, $A^{pq}(r)$, $B^{pq}(r)$, $\bar{C}^{pq}(r)$, $a_{11}^{opq}(r)$, $a_{12}^{opq}(r)$, $a_{12}^{opq}(r)$, $a_3^{opq}(r)$, $\bar{b}_{23}^{opq}(r)$, $\bar{b}_{22}^{opq}(r)$ and $\bar{b}_{21}^{opq}(r)$ are functions of r and $\bar{\cdot}$ represents pseudoscalar.

According to (2.1) and (A1), the equation for the correlation function of magnetic helicity $R^{H_M}(\boldsymbol{r}) = R_{ii}^{ab}(\boldsymbol{r}) = \langle a_i(\boldsymbol{x}) b_i(\boldsymbol{x}')\rangle$ can be written as

$$\partial_t R^{H_M}(r) = \langle \boldsymbol{b}' \cdot \mathcal{E}\rangle + \langle \boldsymbol{a} \cdot \boldsymbol{f}_b{}'\rangle - \eta\langle \boldsymbol{a} \cdot (-\Delta)^{\alpha} \boldsymbol{b}'\rangle + \lambda_b \langle \boldsymbol{a} \cdot \Delta^{-1} \boldsymbol{b}'\rangle, \tag{A3}$$

where $\mathcal{E} = \boldsymbol{U} \times \boldsymbol{b}$, and the superscript $'$ represents the quantities at $\boldsymbol{x}'$. This equation is related to the homogeneous results given by Banerjee & Galtier (2016*b*). In the statistically steady state, $\partial_t R^{H_M}(r) = 0$. With the assumption of isotropy, the nonlinear terms can be written as

$$\begin{aligned} \langle \boldsymbol{b}' \cdot \mathcal{E}\rangle &= R_{ii}^{\mathcal{E}b} = \frac{1}{r^2}\partial_r\left[r^3 R_{LL}^{\mathcal{E}b}\right] \\ &= \frac{1}{r^2}\partial_r\left[r^3\left(\Phi_{23L}^{Ubb} - \Phi_{32L}^{Ubb}\right)\right], \end{aligned} \tag{A4}$$

where the subscript L refers to the longitudinal direction (along $\boldsymbol{r}$), and the subscripts 2 and 3 refer to the two remaining transverse directions. If the forcing and the dissipation terms are also isotropic, according to the results of Xie & Bühler (2019), it can be further derived that

$$\frac{1}{r^2}\partial_r\left[r^3\left(\Phi_{23L}^{Ubb} - \Phi_{32L}^{Ubb}\right)\right] = \int_0^{\infty} \mathrm{d}K \frac{\mathrm{d}F}{\mathrm{d}K}\frac{\sin Kr}{Kr}, \tag{A5}$$

where $F = -\varepsilon_{HMI} + \sum_{k' \in \{k_f\}} \varepsilon_M(k') H(K - k')$, ε_{HMI} is the inverse magnetic helicity flux, $\varepsilon_M(k')$ is the magnetic helicity injection at the forcing wavenumber and $H(K - k')$ is the Heaviside function. The integral of (A5) leads to

$$r\left(\Phi_{23L}^{Ubb}(\boldsymbol{r}) - \Phi_{32L}^{Ubb}(\boldsymbol{r})\right) = \frac{1}{3}\varepsilon_{HMI} r - \sum_{K=k_f} \varepsilon_M(K)\frac{\sin Kr - Kr\cos Kr}{K^3 r^2}. \tag{A6}$$

The equation can also be written in structure function form as

$$\begin{aligned} V_{HM1} &= \frac{r}{2}\langle \delta(U_3 b_2 - U_2 b_3)\delta b_L\rangle \\ &= \frac{1}{3}\varepsilon_{HMI} r - \sum_{K=k_f} \varepsilon_M(K)\frac{\sin Kr - Kr\cos Kr}{K^3 r^2}, \end{aligned} \tag{A7}$$

where $\delta q_i = q_i(\boldsymbol{x}') - q_i(\boldsymbol{x})$ is the two-point increment for an arbitrary vector $\boldsymbol{q}$.

https://doi.org/10.1017/jfm.2025.10559 Published online by Cambridge University Press

A.2. *Alternative formulation of the vKH relation for magnetic helicity*

For a homogeneous quantity $p(\boldsymbol{x})$, there is a relation between $\partial_{\boldsymbol{x}}$, $\partial_{\boldsymbol{x}'}$ and $\partial_{\boldsymbol{r}}$

$$-\partial_{x_i'}\langle p\rangle = \partial_{r_i}\langle p\rangle = \partial_{x_i}\langle p\rangle\,. \tag{A8}$$

Utilising this relation (A8), $\Phi^{vbb}_{lmj}(\boldsymbol{r})$ can be written as

$$\Phi^{vbb}_{lmj}(\boldsymbol{r}) = \epsilon_{jkn}\partial_{r_k}\Phi^{vba}_{lmn}(\boldsymbol{r}). \tag{A9}$$

The isotropic third-order structure function $\Phi^{vba}_{lmn}(\boldsymbol{r}) = \langle v_l b_m a_n'\rangle$ is a pseudo-vector, and can be written as

$$\begin{aligned}\Phi^{vba}_{lmn}(\boldsymbol{r}) = {}& \bar{a}^{vba}_{11}(r)r_n\delta_{lm} + \bar{a}^{vba}_{12}(r)r_m\delta_{ln} + \bar{a}^{vba}_{13}(r)r_l\delta_{mn}\\ &+ \bar{a}^{vba}_{3}(r)r_l r_m r_n + b^{vba}_{23}(r)r_l\varepsilon_{mnp}r_p + b^{vba}_{22}r_m\epsilon_{nlp}r_p\\ &+ b^{vba}_{21}(r)r_n\epsilon_{lmp}r_p.\end{aligned} \tag{A10}$$

According to the relation $\partial_{r_k} = (r_k/r)\partial_r$, for the first three terms, the partial derivatives can be written as

$$\begin{aligned}&\epsilon_{jkn}\partial_{r_k}\left[\bar{a}^{vba}_{11}(r)r_n\delta_{lm} + \bar{a}^{vba}_{12}(r)r_m\delta_{ln} + \bar{a}^{vba}_{13}(r)r_l\delta_{mn}\right]\\ =&\epsilon_{jkn}\left[\left(\partial_r\bar{a}^{vba}_{11}\right)\frac{r_k r_n}{r}\delta_{lm} + \bar{a}^{vba}_{11}\delta_{kn}\delta_{lm}\right.\\ &+\left(\partial_r\bar{a}^{vba}_{12}\right)\frac{r_k r_m}{r}\delta_{ln} + \bar{a}^{vba}_{12}\delta_{km}\delta_{ln}\\ &\left.+\left(\partial_r\bar{a}^{vba}_{13}\right)\frac{r_k r_l}{r}\delta_{mn} + \bar{a}^{vba}_{13}\delta_{kl}\delta_{mn}\right]\\ =&\epsilon_{jkl}\left(\partial_r\bar{a}^{vba}_{12}\right)\frac{r_k r_m}{r} + \epsilon_{jml}\bar{a}^{vba}_{12}\\ &+\epsilon_{jkm}\left(\partial_r\bar{a}^{vba}_{13}\right)\frac{r_k r_l}{r} + \epsilon_{jlm}\bar{a}^{vba}_{13}.\end{aligned} \tag{A11}$$

If $\{l, m, j\} = \{2, 3, L\}$, then $r_l = r_m = 0$. In addition, there are two relations

$$\begin{aligned}\bar{a}^{vba}_{13}(r)r &= \Phi^{vba}_{L22}(\boldsymbol{r}) = \Phi^{vba}_{L33}(\boldsymbol{r}),\\ \bar{a}^{vba}_{12}(r)r &= \Phi^{vba}_{2L2}(\boldsymbol{r}) = \Phi^{vba}_{3L3}(\boldsymbol{r}).\end{aligned} \tag{A12}$$

Therefore, (A11) can be further simplified as

$$\begin{aligned}&\epsilon_{jkn}\partial_{r_k}\left[\bar{a}^{vba}_{11}(r)r_n\delta_{lm} + \bar{a}^{vba}_{12}(r)r_m\delta_{ln} + \bar{a}^{vba}_{13}(r)r_l\delta_{mn}\right]\Big|_{\{l,m,j\}=\{2,3,L\}}\\ &= \bar{a}^{vba}_{13}(r) - \bar{a}^{vba}_{12}(r) = \Phi^{vba}_{L22}(\boldsymbol{r}) - \Phi^{vba}_{2L2}(\boldsymbol{r}).\end{aligned} \tag{A13}$$

By similar derivation, the curls of the other four terms in (A10) are zero

$$\begin{aligned}&\epsilon_{jkn}\partial_{r_k}\left[\bar{a}^{vba}_{3}(r)r_l r_m r_n + b^{vba}_{23}(r)r_l\varepsilon_{mnp}r_p + b^{vba}_{22}r_m\epsilon_{nlp}r_p\right.\\ &\left.+ b^{vba}_{21}(r)r_n\epsilon_{lmp}r_p\right]\Big|_{\{l,m,j\}=\{2,3,L\}} = 0.\end{aligned} \tag{A14}$$

Therefore, it can be obtained from (A9), (A10), (A13) and (A14) that

$$\Phi^{vbb}_{23L}(\boldsymbol{r}) = \left(\Phi^{vba}_{L22}(\boldsymbol{r}) - \Phi^{vba}_{2L2}(\boldsymbol{r})\right)/r. \tag{A15}$$

https://doi.org/10.1017/jfm.2025.10559 Published online by Cambridge University Press

It can be derived from (A2) that

$$\Phi_{23L}^{vbb}(\boldsymbol{r}) = -\Phi_{32L}^{vbb}(\boldsymbol{r}) = r^2 \bar{b}_{21}(r). \tag{A16}$$

Therefore, (A15) can be rewritten as

$$r\big(\Phi_{23L}^{vbb}(\boldsymbol{r}) - \Phi_{32L}^{vbb}(\boldsymbol{r})\big) = 2\big(\Phi_{L22}^{vba}(\boldsymbol{r}) - \Phi_{2L2}^{vba}(\boldsymbol{r})\big). \tag{A17}$$

Now, we concentrate on the alternative form of the Hall effects: $-d_I r(\Phi_{23L}^{jbb}(\boldsymbol{r}) - \Phi_{32L}^{jbb}(\boldsymbol{r}))$.

Using $(\nabla \times \boldsymbol{b}) \times \boldsymbol{b} = (\boldsymbol{b} \cdot \nabla)\boldsymbol{b} - \nabla|\boldsymbol{b}|^2/2$ and (A8), there are following relations:

$$\Phi_{23L}^{jbb}(\boldsymbol{r}) - \Phi_{32L}^{jbb}(\boldsymbol{r}) = -\partial_{r_i}\Phi_{LiL}^{bbb}(\boldsymbol{r}) + \frac{1}{2}\partial_{r_L}\Phi_{iiL}^{bbb}(\boldsymbol{r}). \tag{A18}$$

According to (A2), $\Phi_{LiL}^{bbb}(\boldsymbol{r})$ can be written as

$$\Phi_{LiL}^{bbb}(\boldsymbol{r}) = \bar{a}_{11}^{bbb}(r) r_L \delta_{Li} + \bar{a}_{12}^{bbb}(r) r_i + \bar{a}_{13}^{bbb}(r) r_L \delta_{iL} + \bar{a}_3(r)^{bbb} r^2 r_i. \tag{A19}$$

Then, $\partial_{r_i}\Phi_{LiL}^{bbb}(\boldsymbol{r})$ in (A18) can be written as

$$\begin{aligned}\partial_{r_i}\Phi_{LiL}^{bbb}(\boldsymbol{r}) = {} & r\partial_r \bar{a}_{11}^{bbb}(r) + \bar{a}_{11}^{bbb}(r) + r\partial_r \bar{a}_{12}^{bbb}(r) \\ & + 3\bar{a}_{12}^{bbb}(r) + r\partial_r \bar{a}_{13}^{bbb}(r) + \bar{a}_{13}^{bbb}(r) \\ & + r^3 \partial_r \bar{a}_3^{bbb}(r) + 5r^2 \bar{a}_3^{bbb}(r).\end{aligned} \tag{A20}$$

For incompressible flow, there are the following relations for isotropic third-order structure functions (Politano *et al.* 2003):

$$\begin{cases} r\partial_r \bar{a}_{11}^{bbb}(r) + 3\bar{a}_{11}^{bbb}(r) + \bar{a}_{12}^{bbb}(r) + \bar{a}_{13}^{bbb}(r) = 0, \\ \dfrac{1}{r}\big(\partial_r \bar{a}_{12}^{bbb}(r) + \partial_r \bar{a}_{13}^{bbb}(r)\big) + r\partial_r \bar{a}_3^{bbb}(r) + 5\bar{a}_3^{bbb}(r) = 0, \\ 3\bar{a}_{11}^{bbb}(r) + \bar{a}_{12}^{bbb}(r) + \bar{a}_{13}^{bbb}(r) + r^2 \bar{a}_3^{bbb}(r) = 0. \end{cases} \tag{A21}$$

Using these relations, (A20) can be simplified as

$$\partial_{r_i}\Phi_{LiL}^{bbb}(\boldsymbol{r}) = \frac{1}{r}\Phi_{Lii}^{bbb}(\boldsymbol{r}). \tag{A22}$$

According to the incompressible relation (A21), $\partial_{r_L}\Phi_{iiL}^{bbb}(\boldsymbol{r})$ in (A18) can be derived as

$$\partial_{r_L}\Phi_{iiL}^{bbb}(\boldsymbol{r}) = \partial_{r_L}\big\{\big[3\bar{a}_{11}^{bbb}(r) + \bar{a}_{12}^{bbb}(r) + \bar{a}_{13}^{bbb}(r) + \bar{a}_3^{bbb}(r) r^2\big] r_L\big\} = 0. \tag{A23}$$

Then, according to (A18), (A22), and (A23), the Hall effects can be rewritten as

$$-d_I r\big(\Phi_{23L}^{jbb}(\boldsymbol{r}) - \Phi_{32L}^{jbb}(\boldsymbol{r})\big) = d_I \Phi_{Lii}^{bbb}(\boldsymbol{r}). \tag{A24}$$

According to (A17) and (A24), the alternative formulation for vKH relations can be written as

$$r\big(\Phi_{23L}^{Ubb}(\boldsymbol{r}) - \Phi_{32L}^{Ubb}(\boldsymbol{r})\big) = 2\big[\Phi_{L22}^{vba}(\boldsymbol{r}) - \Phi_{2L2}^{vba}(\boldsymbol{r})\big] + d_I \Phi_{Lii}^{bbb}(\boldsymbol{r}). \tag{A25}$$

https://doi.org/10.1017/jfm.2025.10559 Published online by Cambridge University Press

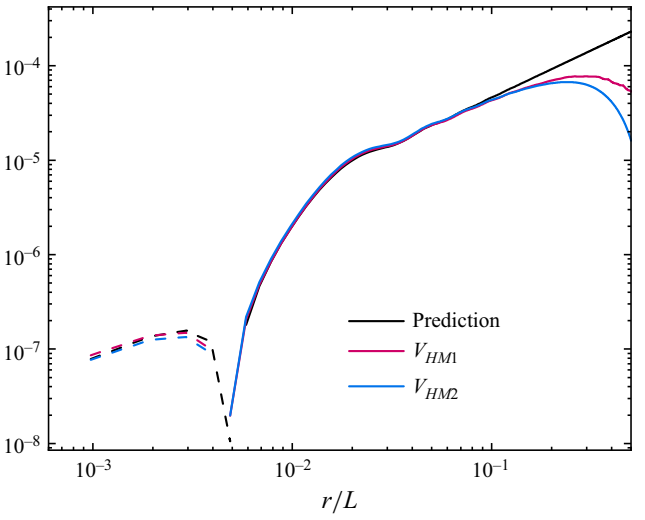


Figure 15. Numerical verifications of V_{HM1} and V_{HM2} using H40. Solid lines: positive values; dashed lines: negative values.

The above vKH relations can be written in two-point increments and averages. For example, $\Phi^{vba}_{L22}(\boldsymbol{r})$ can be replaced by $-\langle\delta(v_L b_2)a_2^*\rangle$

$$\begin{aligned}\left\langle\delta(v_L b_2)a_2^*\right\rangle &= \left\langle v_L(\boldsymbol{x}')b_2(\boldsymbol{x}')a_2(\boldsymbol{x}) - v_L(\boldsymbol{x})b_2(\boldsymbol{x})a_2(\boldsymbol{x}')\right\rangle/2\\ &= \left\langle v_L(\boldsymbol{x})b_2(\boldsymbol{x})a_2(\boldsymbol{x}-\boldsymbol{r}) - v_L(\boldsymbol{x})b_2(\boldsymbol{x})a_2(\boldsymbol{x}')\right\rangle/2\\ &= \left[\Phi^{vba}_{L22}(-\boldsymbol{r}) - \Phi^{vba}_{L22}(\boldsymbol{r})\right]/2 = -r\bar{a}^{vba}_{13}(r)\\ &= -\Phi^{vba}_{L22}(\boldsymbol{r}),\end{aligned} \tag{A26}$$

where $q_i^*(\boldsymbol{r}) = [q_i(\boldsymbol{x}) + q_i(\boldsymbol{x}')]/2$ for an arbitrary vector $\boldsymbol{q}$. Using two-point increments and averages, the right-hand side of (A25) can be written as

$$V_{HM2} = 2\left\langle\delta(v_2 b_L - v_L b_2)a_2^*\right\rangle - d_I\left\langle\delta(b_L b_i)b_i^*\right\rangle. \tag{A27}$$

In conclusion, (A7) and (A27) give two estimations for magnetic helicity cascade rates. Figure 15 verifies the two vKH relations using the results of H40, where black curves are predictions in (A7), with $\varepsilon_{HMI} = 4.4\times10^{-4}$ and $\varepsilon_M = 5.4\times10^{-4}/3$.

Considering that the potential $\boldsymbol{a}$ and current density $\boldsymbol{j}$ are hard to be obtained in solar wind observation, V_{HM1} and V_{HM2} can be combined as

$$V_{HM} = \frac{r}{2}\langle\delta(v_3 b_2 - v_2 b_3)\delta b_L\rangle - d_I\left\langle\delta(b_L b_i)b_i^*\right\rangle, \tag{A28}$$

where $\delta q_i = q_i(\boldsymbol{x}') - q_i(\boldsymbol{x})$ is the two-point increment for an arbitrary vector $\boldsymbol{q}$.

References

ALEXAKIS, A. 2013 Large-scale magnetic fields in magnetohydrodynamic turbulence. *Phys. Rev. Lett.* **110**, 084502.

ALEXAKIS, A. 2017 Helically decomposed turbulence. *J. Fluid Mech.* **812**, 752–770.

ALEXAKIS, A. & BIFERALE, L. 2018 Cascades and transitions in turbulent flows. *Phys. Rep.* **767–769**, 1–101.

ALUIE, H. 2017 Coarse-grained incompressible magnetohydrodynamics: analyzing the turbulent cascades. *New J. Phys.* **19**, 025008.

ALUIE, H. & EYINK, G.L. 2010 Scale locality of magnetohydrodynamic turbulence. *Phys. Rev. Lett.* **104**, 081101.

https://doi.org/10.1017/jfm.2025.10559 Published online by Cambridge University Press

BALE, S.D., *et al.* 2016 The FIELDS instrument suite for solar probe plus. *Space Sci. Rev.* **204**, 49–82.
BANDYOPADHYAY, R., *et al.* 2018 Solar wind turbulence studies using MMS fast plasma investigation data. *Astrophys. J.* **866**, 81.
BANDYOPADHYAY, R., *et al.* 2020 Enhanced energy transfer rate in solar wind turbulence observed near the sun from parker solar probe. *Astrophys. J. Suppl. Ser.* **246**, 48.
BANERJEE, S. & GALTIER, S. 2016*a* An alternative formulation for exact scaling relations in hydrodynamic and magnetohydrodynamic turbulence. *J. Phys. A: Math. Theor.* **50**, 015501.
BANERJEE, S. & GALTIER, S. 2016*b* Chiral exact relations for helicities in Hall magnetohydrodynamic turbulence. *Phys. Rev. E* **93**, 033120.
BERESNYAK, A. 2018 The rate of three-dimensional Hall-MHD reconnection. *J. Phys.: Conf. Ser.* **1031**, 012001.
BHATTACHARJEE, A. 2004 Impulsive magnetic reconnection in the earth's magnetotail and the solar corona. *Annu. Rev. Astron. Astrophys.* **42**, 365–384.
BIAN, X. & ALUIE, H. 2019 Decoupled cascades of kinetic and magnetic energy in magnetohydrodynamic turbulence. *Phys. Rev. Lett.* **122**, 135101.
BIFERALE, L., MUSACCHIO, S. & TOSCHI, F. 2012 Inverse energy cascade in three-dimensional isotropic turbulence. *Phys. Rev. Lett.* **108**, 164501.
BIFERALE, L., MUSACCHIO, S. & TOSCHI, F. 2013 Split energy–helicity cascades in three-dimensional homogeneous and isotropic turbulence. *J. Fluid Mech.* **730**, 309–327.
BOLDYREV, S. 2005 On the spectrum of magnetohydrodynamic turbulence. *Astrophys. J.* **626**, L37.
BOLDYREV, S. 2006 Spectrum of magnetohydrodynamic turbulence. *Phys. Rev. Lett.* **96**, 115002.
BRODIANO, M., DMITRUK, P. & ANDRÉS, N. 2023 A statistical study of the compressible energy cascade rate in solar wind turbulence: Parker solar probe observations. *Phys. Plasmas* **30**, 032903.
BRUNO R., CARBONE V., CHAPMAN S., HNAT B., NOULLEZ A. & SORRISO-VALVO L. 2007 Intermittent character of interplanetary magnetic field fluctuations. *Phys. Plasmas* **14**, 032901.
BRUNO, R., CARBONE, V., PRIMAVERA, L., MALARA, F., SORRISO-VALVO, L., BAVASSANO, B. & VELTRI, P. 2004 On the probability distribution function of small-scale interplanetary magnetic field fluctuations. *Ann. Geophys.* **22**, 3751–3769.
BUZZICOTTI, M., ALUIE, H., BIFERALE, L. & LINKMANN, M. 2018 Energy transfer in turbulence under rotation. *Phys. Rev. Fluids* **3**, 034802.
CAMPOREALE, E., SORRISO-VALVO, L., CALIFANO, F. & RETINÒ, A. 2018 Coherent structures and spectral energy transfer in turbulent plasma: a space-filter approach. *Phys. Rev. Lett.* **120**, 125101.
CASE, A.W., *et al.* 2020 The solar probe cup on the parker solar probe. *Astrophys. J. Suppl. Ser.* **246**, 43–54.
CHANDRAN, B.D.G., SCHEKOCHIHIN, A.A. & MALLET, A. 2015 Intermittency and alignment in strong RMHD turbulence. *Astrophys. J.* **807**, 39–54.
CHEN, C.H.K., *et al.* 2020 The evolution and role of solar wind turbulence in the inner heliosphere. *Astrophys. J. Suppl. Ser.* **246**, 53–62.
CHEN Q., CHEN S. & EYINK G.L. 2003 The joint cascade of energy and helicity in three-dimensional turbulence. *Phys. Fluids* **15**, 361–374.
DE KARMAN, T. & HOWARTH, L. 1938 On the statistical theory of isotropic turbulence. *Proc. R. Soc. Lond. A: Math. Phys. Sci.* **164**, 192–215,
DORELLI, J.C., GLOCER, A., COLLINSON, G. & TÓTH, G. 2015, The role of the Hall effect in the global structure and dynamics of planetary magnetospheres: Ganymede as a case study. *J. Geophys. Res.: Space Phys.* **120**, 5377–5392.
EBRAHIMI, F. & RAMAN, R. 2015 Plasmoids formation during simulations of coaxial helicity injection in the national spherical torus experiment. *Phys. Rev. Lett.* **114**, 205003.
ELSASSER, W.M. 1956 Hydromagnetic dynamo theory. *Rev. Mod. Phys.* **28**, 135–163.
FAGANELLO, M., CALIFANO, F. & PEGORARO, F. 2008 Time window for magnetic reconnection in plasma configurations with velocity shear. *Phys. Rev. Lett.* **101**, 175003.
FERRAND, R., GALTIER, S., SAHRAOUI, F., MEYRAND, R., ANDRÉS, N. & BANERJEE, S. 2019 On exact laws in incompressible hall magnetohydrodynamic turbulence. *Astrophys. J.* **881**, 50–55.
FOX, N.J., *et al.* 2016 The solar probe plus mission: humanity's first visit to our star. *Space Sci. Rev.* **204**, 7–48.
FRISCH, U., POUQUET, A., LÉORAT, J. & MAZURE, A. 1975 Possibility of an inverse cascade of magnetic helicity in magnetohydrodynamic turbulence. *J. Fluid Mech.* **68**, 769–778.
GALTIER, S. 2006 Wave turbulence in incompressible Hall magnetohydrodynamics. *J. Plasma Phys.* **72**, 721–769.
GALTIER, S. 2008 von Kármán–Howarth equations for Hall magnetohydrodynamic flows. *Phys. Rev. E* **77**, 015302.

https://doi.org/10.1017/jfm.2025.10559 Published online by Cambridge University Press

GALTIER, S. 2016 *Introduction to Modern Magnetohydrodynamics*. Cambridge University Press.
GARY, S.P. & SMITH, C.W. 2009 Short-wavelength turbulence in the solar wind: Linear theory of whistler and kinetic Alfvén fluctuations. *J. Geophys. Res.: Space Phys.* **114**, 2009JA014525.
GOLDREICH, P. & SRIDHAR, S. 1997 Magnetohydrodynamic turbulence revisited. *Astrophys. J.* **485**, 680–688.
GRECO, A., MATTHAEUS, W.H., SERVIDIO, S., CHUYCHAI, P. & DMITRUK, P.2009 Statistical analysis of discontinuities in solar wind ace data and comparison with intermittent mhd turbulence. *Astrophys. J. Lett.* **691**, L111–L114.
HELLINGER, P., VERDINI, A., LANDI, S., FRANCI, L. & MATTEINI, L. 2018 von kármán–Howarth equation for hall magnetohydrodynamics: hybrid simulations. *Astrophys. J. Lett.* **857**, L19–L23.
HU, R., LI, X. & YU, C. 2022 Transfers of energy and helicity in helical rotating turbulence. *J. Fluid Mech.* **946**, A19.
KIYANI, K.H., CHAPMAN, S.C., KHOTYAINTSEV, YU V., DUNLOP, M.W. & SAHRAOUI, F. 2009 Global scale-invariant dissipation in collisionless plasma turbulence. *Phys. Rev. Lett.* **103**, 075006.
KOLMOGOROV, A.N. 1941 *Dokl. Akad. Nauk SSSR* **30**, 299–303.
KUZZAY, D., ALEXANDROVA, O. & MATTEINI, L. 2019 Local approach to the study of energy transfers in incompressible magnetohydrodynamic turbulence. *Phys. Rev. E* **99**, 053202.
LINKMANN, M. & DALLAS, V. 2017 Triad interactions and the bidirectional turbulent cascade of magnetic helicity. *Phys. Rev. Fluids* **2**, 054605.
MANZINI, D., SAHRAOUI, F., CALIFANO, F. & FERRAND, R. 2022 Local energy transfer and dissipation in incompressible Hall magnetohydrodynamic turbulence: the coarse-graining approach. *Phys. Rev. E* **106**, 035202.
MARCHAND, P., TOMIDA, K., COMMERÇON, B. & CHABRIER, G. 2019 Impact of the Hall effect in star formation, improving the angular momentum conservation. *Astron. Astrophys.* **631** , A66.
MARINO, R. & SORRISO-VALVO, L. 2023 Scaling laws for the energy transfer in space plasma turbulence. *Phys. Rep.* **1006**, 1–144.
MARINO, R., SORRISO-VALVO, L., CARBONE, V., VELTRI, P., NOULLEZ, A. & BRUNO, R. 2011 The magnetohydrodynamic turbulent cascade in the ecliptic solar wind: study of Ulysses data. *Planet. Space Sci.* **59**, 592–597.
MARINO, R., SORRISO-VALVO, L., D'AMICIS, R., CARBONE, V., BRUNO, R. & VELTRI, P. 2012 On the occurrence of the third-order scaling in high latitude solar wind. *Astrophys. J.* **750**, 41–48.
MARTIN, L.N., DE VITA, G., SORRISO-VALVO, L., DMITRUK, P., NIGRO, G., PRIMAVERA, L. & CARBONE, V. 2013 Cancellation properties in Hall magnetohydrodynamics with a strong guide magnetic field. *Phys. Rev. E* **88**, 063107.
MASON, J., CATTANEO, F. & BOLDYREV, S. 2008 Numerical measurements of the spectrum in magnetohydrodynamic turbulence. *Phys. Rev. E* **77**, 036403.
MATTHAEUS, W.H. & GOLDSTEIN, M.L. 1982 Measurement of the rugged invariants of magnetohydrodynamic turbulence in the solar wind. *J. Geophys. Res.: Space Phys.* **87**, 6011–6028.
MILANESE L.M., LOUREIRO N.F. & BOLDYREV S. 2021 Dynamic phase alignment in Navier–Stokes turbulence. *Phys. Rev. Lett.* **127**, 274501.
MININNI, P.D., GOMEZ, D.O. & MAHAJAN, S.M. 2005 Direct simulations of helical Hall-MHD turbulence and dynamo action. *Astrophys. J.* **619**, 1019.
MIURA H. 2024 Formation of fine structures in incompressible hall magnetohydrodynamic turbulence simulations. *Plasma* **7**, 793–815.
MIURA, H. & ARAKI, K. 2014 Structure transitions induced by the Hall term in homogeneous and isotropic magnetohydrodynamic turbulence. *Phys. Plasmas* **21**, 072313.
MÜLLER, W.-C., MALAPAKA, S.K. & BUSSE, A. 2012 Inverse cascade of magnetic helicity in magnetohydrodynamic turbulence. *Phys. Rev. E* **85**, 015302.
OSMAN, K.T., MATTHAEUS, W.H., WAN, M. & RAPPAZZO, A.F. 2012 Intermittency and local heating in the solar wind. *Phys. Rev. Lett.* **108**, 261102.
OSMAN, K.T., WAN, M., MATTHAEUS, W.H., BREECH, B. & OUGHTON, S. 2011 Directional alignment and non-Gaussian statistics in solar wind turbulence. *Astrophys. J.* **741**, 75–79.
PEREZ, J.C., MASON, J., BOLDYREV, S. & CATTANEO, F. 2012 On the energy spectrum of strong magnetohydrodynamic turbulence. *Phys. Rev. X* **2**, 041005.
PLUNIAN, F., TEIMURAZOV, A., STEPANOV, R. & VERMA, M.K. 2020 Inverse cascade of energy in helical turbulence. *J. Fluid Mech.* **895**, A13.
PODESTA, J.J., ROBERTS, D.A. & GOLDSTEIN, M.L. 2007 Spectral exponents of kinetic and magnetic energy spectra in solar wind turbulence. *Astrophys. J.* **664**, 543.

https://doi.org/10.1017/jfm.2025.10559 Published online by Cambridge University Press

POLITANO, H., GOMEZ, T. & POUQUET, A. 2003 von Kármán–Howarth relationship for helical magnetohydrodynamic flows. *Phys. Rev. E* **68**, 026315.
POLITANO, H. & POUQUET, A. 1998 Dynamical length scales for turbulent magnetized flows. *Geophys. Res. Lett.* **25**, 273–276.
POPE, S.B. 2000 *Turbulent Flows*. Cambridge University Press.
POUQUET, A., ROSENBERG, D., STAWARZ, JE & MARINO, R. 2019 Helicity dynamics, inverse, and bidirectional cascades in fluid and magnetohydrodynamic turbulence: a brief review. *Earth Space Sci.* **6**, 351–369.
RAOUAFI, N.E., *et al.* 2023 Parker solar probe: four years of discoveries at solar cycle minimum. *Space Sci. Rev.* **219**, 8.
RICHNER, N.J., BODNER, G.M., BONGARD, M.W., FONCK, R.J., NORNBERG, M.D. & REUSCH, J.A. 2022 Magnetic turbulence and current drive during local helicity injection. *Phys. Rev. Lett.* **128**, 105001.
SAHOO, G. & BIFERALE, L. 2015 Disentangling the triadic interactions in Navier–Stokes equations. *Eur. Phys. J. E* **38**, 1–8.
SALEM, C., MANGENEY, A., BALE, S.D. & VELTRI, P. 2009 Solar wind magnetohydrodynamics turbulence: anomalous scaling and role of intermittency. *Astrophys. J.* **702**, 537–553.
SCHEKOCHIHIN, A.A. 2022 MHD turbulence: a biased review. *J. Plasma Phys.* **88**, 155880501.
SERVIDIO, S., MATTHAEUS, W.H., SHAY, M.A., CASSAK, P.A. & DMITRUK, P. 2009 Magnetic reconnection in two-dimensional magnetohydrodynamic turbulence. *Phys. Rev. Lett.* **102**, 115003.
SMITH, C.W., STAWARZ, J.E., VASQUEZ, B.J., FORMAN, M.A. & MACBRIDE, B.T. 2009 Turbulent cascade at 1 AU in high cross-helicity flows. *Phys. Rev. Lett.* **103**, 201101.
SORRISO-VALVO, L., MARINO, R., CARBONE, V., NOULLEZ, A., LEPRETI, F., VELTRI, P., BRUNO, R., BAVASSANO, B. & PIETROPAOLO, E. 2007 Observation of inertial energy cascade in interplanetary space plasma. *Phys. Rev. Lett.* **99**, 115001.
SORRISO-VALVO, L., MARINO, R., LIJOI, L., PERRI, S. & CARBONE, V. 2015 Self-consistent castaing distribution of solar wind turbulent fluctuations. *Astrophys. J.* **807**, 86–92.
SUN, H., YANG, Y., LU, Q., LU, S., WAN, M. & WANG, R. 2022 Physical regimes of two-dimensional mhd turbulent reconnection in different lundquist numbers. *Astrophys. J.* **926**, 97–110.
TAYLOR, G.I. 1938 The spectrum of turbulence. *Proc. R. Soc. Lond. A: Math. Phys. Sci.* **164**, 476–490.
VELTRI, P. & MANGENEY, A. 1999 Scaling laws and intermittent structures in solar wind MHD turbulence. *AIP Conf. Proc.* **471**, 543–546.
WAN, M., MATTHAEUS, W.H., ROYTERSHTEYN, V., KARIMABADI, H., PARASHAR, T., WU, P. & SHAY, M. 2015 Intermittent dissipation and heating in 3D kinetic plasma turbulence. *Phys. Rev. Lett.* **114**, 175002.
WANG, Y. & CHKHETIANI, O. 2023 Four-thirds law of energy and magnetic helicity in electron and Hall magnetohydrodynamic fluids. *Physica D: Nonlinear Phenom.* **454**, 133835.
WOLTJER, L. 1958 A theorem on force-free magnetic fields. *Proc. Natl Acad. Sci. USA* **44**, 489–491.
WURSTER, J., BATE, M.R. & BONNELL, I.A. 2021 The impact of non-ideal magnetohydrodynamic processes on discs, outflows, counter-rotation, and magnetic walls during the early stages of star formation. *Mon. Not. R. Astron. Soc.* **507**, 2354–2372.
XIE, J.-H. & BÜHLER, O. 2019 Third-order structure functions for isotropic turbulence with bidirectional energy transfer. *J. Fluid Mech.* **877**, R3.
YADAV S.K., MIURA H. & PANDIT R. 2022 Statistical properties of three-dimensional Hall magnetohydrodynamics turbulence. *Phys. Fluids* **34**, 095135.
YAN, Z., LI, X., YU, C., WANG, J. & CHEN, S. 2020 Dual channels of helicity cascade in turbulent flows. *J. Fluid Mech.* **894**, R2.

https://doi.org/10.1017/jfm.2025.10559 Published online by Cambridge University Press